

LETTER TO THE EDITOR

Cosmic Ray Electrons Accounting for the North Polar Spur and the Acceleration Efficiency of Weak Shocks

Guobin Mou¹, Jianhao Wu², and Yoshiaki Sofue³

¹ School of Physics and Technology, Wuhan University, Wuhan 430072, China
e-mail: gbmou@whu.edu.cn

² School of Computer Science, Wuhan University, Wuhan 430072, China
e-mail: jianhao.wu@whu.edu.cn

³ Institute of Astronomy, The University of Tokyo, Mitaka, Tokyo 181-0015, Japan

ABSTRACT

Aims. The parameters of cosmic ray electrons (CRE) and the strength of magnetic field are crucial for studying particle acceleration of shocks. The recent discovery of eROSITA bubbles suggests that the well-known NPS/Loop I should be a 10-kpc sized relic in the Galactic halo instead of a small local structure near the Sun. By deriving the energy density of CRE and magnetic field strength accounting for the NPS, unprecedentedly precise parameter constraints on particle acceleration for weak shocks in halo medium can be provided.

Methods. The parameters of CRE and magnetic field can be derived independently by modeling the gamma-ray and the radio data of the NPS via inverse Compton scattering and synchrotron emission, respectively.

Results. Our main results are: (1), **the energy density of CRE is $(2-5) \times 10^{-14}$ erg cm⁻³, and the spectral index is $p \approx 2.0 \pm 0.1$** ; (2), **the magnetic field strength is 4 μ G**; (3), **the shock acceleration efficiency of CRE is close to 1%**. Given the Mach number of 1.5, the high acceleration efficiency and flat spectrum of CRE suggest that re-acceleration of preexisting relativistic electrons should exist in the NPS. In addition, CRE population steepens at a cooling break of ~ 4 GeV, of which the cooling timescale is 10^7 yr, in agreement with the eROSITA bubbles' age.

Key words. acceleration of particles - radiation mechanisms: non-thermal - galaxies: clusters: general - shock waves

1. Introduction

Particle acceleration for strong shocks is becoming constrained in both SNR observations and numerical simulations (e.g., Morlino & Caprioli 2012; Blasi 2013). However, the efficiency of low-Mach-number (typically $M \lesssim 3$) and high/moderate thermal-to-magnetic pressure ratio environment in intra-galactic-medium or circumgalactic medium remains largely uncertain. According to the diffusive shock acceleration (DSA) mechanism, the acceleration efficiency of CRE η_e is very small, which is a few orders of magnitude lower than that of CRp. However, for some radio relics, the observed radio brightness suggests that η_e should be very high (Kang et al. 2012; Brunetti & Jones 2014; Vazza et al. 2015; Botteon et al. 2020), which does not reconcile with the DSA mechanism (but see also Locatelli et al. 2020 for a radio relic consistent with DSA). Furthermore, given the low-Mach number of the shocks inferred from X-ray observations, radio spectra of some radio relics are significantly flatter than the DSA's prediction (see reviews by Brunetti & Jones 2014; van Weeren et al. 2019). In order to solve these problems, the re-acceleration mechanism is considered in which the preexisting "fossil" relativistic electrons can be efficiently re-accelerated by shocks (Kang & Ryu 2011; Pinzke et al. 2013), and this mechanism is also supported in observations of some merging galaxy clusters (van Weeren et al. 2017; Di Gennaro et al. 2018).

However, samples of distant galaxies/clusters bring large uncertainties to studying the acceleration efficiency due to the narrow range of observable frequencies, the coupling between the

parameter of CRE and magnetic field strength for the radio emission, and the difficulty in measuring the field strength. One may adopt the energy equipartition method to derive the distribution of CRE and magnetic field, which however involves major uncertainties since the energy ratio between CRp and CRE is largely unknown (Beck & Krause 2005). Thus, a source with rich observational data especially those breaking the degeneracy between CRE and magnetic field, is crucial in probing the acceleration efficiency of weak shocks.

Loop I, the giant loop spanning almost 100 degrees in the radio sky map, has been known for 60 years (Large et al. 1962). Its eastern part is prominently brighter than its western part, and is called the North Polar Spur (NPS). Loop I/NPS is outstanding in a wide range of frequencies from tens of MHz to tens of GHz (e.g., De Oliveira-Costa et al. 2008), and the lower frequencies of $\lesssim 10^1$ GHz are expected to be dominated by synchrotron emission. Moreover, it is also visible in X-ray (Snowden et al. 1997) and gamma-ray band (Casanjian & Grenier 2009; Su et al. 2010). During the past decades, most literature regarded NPS/Loop I as a local structure (LS) of the order of $\sim 10^2$ parsecs which could originate from an old SNR or stellar activity (Weaver 1979; Wolleben 2007). A recent work (Panopoulou et al. 2021) investigated the optical polarization angles of nearby stars induced by the foreground dust (Das et al. 2020). The starlight polarization angles at Galactic Latitude $b > 30^\circ$ are essentially aligned with that of the radio NPS in tens of GHz, and thereby they argued that this part of the NPS should be located within ~ 100 pc.

Nevertheless, Sofue believes that it could be a large halo structure (HS) of the order of ten kiloparsecs at the galactic center distance (Sofue 1977, 2000; Sofue et al. 2016), which could originate from the past outburst of the Galactic center. This scenario is becoming attractive, as it is consistent with the multi-wavelength structures discovered during the recent decade, including its southern counterpart in X-ray band (Predehl et al. 2020), Fermi bubbles (Su et al. 2010) and polarized radio lobes (Carretti et al. 2013). This is further confirmed in those hydrodynamic simulations modeling the Fermi bubbles (Guo & Mathews 2012; Mou et al. 2014; Sarkar 2019). Due to highly overlapping, the radio Loop I and the northern eROSITA bubble should be the same physical structure, where the radio emission should come from the synchrotron radiation of CRe accelerated by the forward shock. Thus, the discovery of southern eROSITA bubble provides a convincing evidence to support the HS picture, which is also supported by foreground absorption of X-ray by Aquila Rift clouds at a distance of 1 kpc (Sofue 2015; Sofue et al. 2016). We believe that radio and X-ray Loop I/NPS is a GC-distance halo structure, while it is coincidentally overlapped by the foreground local dust and H I. As shown in our recent simulation study (Mou et al. 2022), both the prominent east-west asymmetry of Loop I/NPS and the faintness of its southern counterpart (north-south asymmetry) which frequently raised as supports for the LS scenario, can be caused by a crossing CGM wind injected from the east by north in Galactic coordinates with a velocity of $\sim 200 \text{ km s}^{-1}$ (see also Mou et al. 2018; Sofue 2019 for analytical studies). Inferred from X-rays, the Mach number of NPS/Loop I is ~ 1.5 , and the age of NPS/Loop I should be 10^7 yr (Kataoka et al. 2013; Predehl et al. 2020). In this context, NPS/Loop I, which possibly has been misunderstood for several decades, could be an excellent object for studying the particle acceleration of weak shocks, although it is much smaller than those Mpc-sized radio relics of concern.

The model and result are presented in Section 2, and we discussed the results in Section 3.

2. Model and Result

2.1. Basic Method

For the radio NPS (see Figure 1 for 408 MHz map), our analysis is restricted to latitudes $b > 30^\circ$ to avoid complications near the Galactic plane, which is also in line with the sky region for the gamma-ray data in Jóhannesson & Porter (2021). The temperature spectral index β ($T_B \sim \nu^{-\beta}$) of the NPS is ~ 2.55 between 45 MHz and 408 MHz (Guzmán et al. 2011). It steepens as the frequency increases to GHz: $\beta \sim 2.8$ between 408 MHz and 2.3 GHz (Platania et al. 2003), ~ 3.0 between 408 MHz and 23 GHz (Miville-Deschênes et al. 2008). Vidal et al. (2015) found that β of the NPS is around 3 between 23 and 41 GHz from WMAP data although with a large dispersion, and Jew & Grumitt (2020) found it to be $3 - 3.2$ between 30 and 44 GHz from Planck data. The steepening of the synchrotron spectrum suggests a turning point at $\sim 10^0 \text{ GHz}$, which should be indicative of a cooling break in the CRe population. The main cooling mechanisms of the NPS involve synchrotron or inverse Compton scattering (ICS), which makes the spectral energy distribution (SED) of CRe steeper by one power of γ_e for continuous injection of CRe. Here we assumed a SED of CRe accounting for the NPS in a broken power-law form with the exponential cut-off at

γ_{ct} :

$$\frac{dN_{cre}}{d\gamma_e} = \begin{cases} N_0 \gamma_e^{-p} & (\gamma_e < \gamma_{br}) \\ N_1 \gamma_e^{-p-1} \exp(-\gamma_e/\gamma_{ct}) & (\gamma_e \geq \gamma_{br}) \end{cases} \quad (1)$$

where γ_{br} is the Lorentz factor of the cooling break energy E_{br} . Continuity requires $N_1 = N_0 \gamma_{br}$. **We investigated the cases with $p = 1.9 - 2.2$, and set the exponential cut-off at $\gamma_{ct} = 9.8 \times 10^5$ (0.5 TeV) for $p \leq 2.0$ and 1.96×10^6 (1 TeV) for $p \geq 2.1$ to improve the fitting of gamma-ray spectrum.** For non-relativistic bulk motion which is the case concerned here, the energy distribution peaks at $\gamma_e \sim 2$, as a result of CRe following a power-law distribution in momentum (instead of energy) with slope p (Bell 1978; Sironi et al. 2013). Therefore, the SED of CRe (equation 1) can be regarded as starting from $\gamma_e = 2$ ¹. The only two unknown parameters of CRe population are the coefficients N_0 and N_1 in equation 1.

In this work, we adopted one-zone assumption for simplicity. Due to the coupling between the energy density of CRe and the magnetic field, these parameters cannot be derived from radio data alone. Thanks to the Fermi-LAT, the gamma-ray spectrum of the NPS has been obtained (e.g., Jóhannesson & Porter 2021). The parameters of CRe can be solved independently via fitting the gamma-ray spectrum through ICS of CRe. After that, the magnetic field strength can be derived by fitting the radio spectrum. This is the basic method of this work.

2.2. Geometry Structure

The physical structure of Loop I/NPS is generally regarded as the post-shock medium. Before modeling the radio and gamma-ray NPS, we should know the thickness of the radiative shell along the sightline – $D_s(l, b)$. We adopt 3D Cartesian coordinates, in which Z-axis is the Galactic polar axis, and our solar system is located at $(X, Y, Z) = (0, -8.2 \text{ kpc}, 0)$ (Bland-Hawthorn & Gerhard 2016). We constructed a 3D hollow and thick-shelled bubble in the Galactic halo with its center at $(X_{cnt}, 0, Z_{cnt})$. The inner and outer radii of the shell is R_{in} and R_{out} , respectively, in which we forced $R_{in} = Z_{cnt}$ to reduce degrees of freedom. By testing a series of parameter groups, the four parameters can be estimated by comparing the shell's projection in the Galactic coordinates and the observed NPS. The fitting result is $(R_{in}, R_{out}) = (5.0 \text{ kpc}, 7.5 \text{ kpc})$ and $(X_{cnt}, Z_{cnt}) = (1.5 \text{ kpc}, 5.0 \text{ kpc})$, and the modeled $D_s(l, b)$ is shown in Figure 1. The value of $D_s(l, b)$ depends on the specific direction, but is basically in the range of 6–10 kpc. Here we adopted $D_s(l, b) = 8 \text{ kpc}$ as the fiducial value. For the LS, if we examine the case where the center is 100 pc from the Sun, the projected thickness of the shell can be obtained by $D_s^{LS} = D_s \cdot (100 \text{ pc}/9.4 \text{ kpc}) = 0.011 D_s = 0.88 \text{ kpc}$ with the help of similar-geometry. Thus, the values of the projected thickness under the two physical scenarios differ by two orders of magnitude, which will have a significant impact on the parameters of CRe required to fit the observations.

2.3. Gamma-Ray NPS

There are two possible origins for gamma rays: ICS of interstellar radiation field (ISRF) by CRe, or hadronic origin (pp collisions). If it is hadronic origin, the gamma-ray luminosity per unit volume is $j_\gamma \sim f \sigma_{pp} e_{crp} n_{gas} c$, where $f \sim 0.17$ is the fraction of CRp's kinetic energy transferred into π^0 which instantaneously

¹ When adopting the lower bound of $\gamma_e = 1$ or 2 with $p \leq 2.2$, the difference in the energy density of CRe is only a few percent.

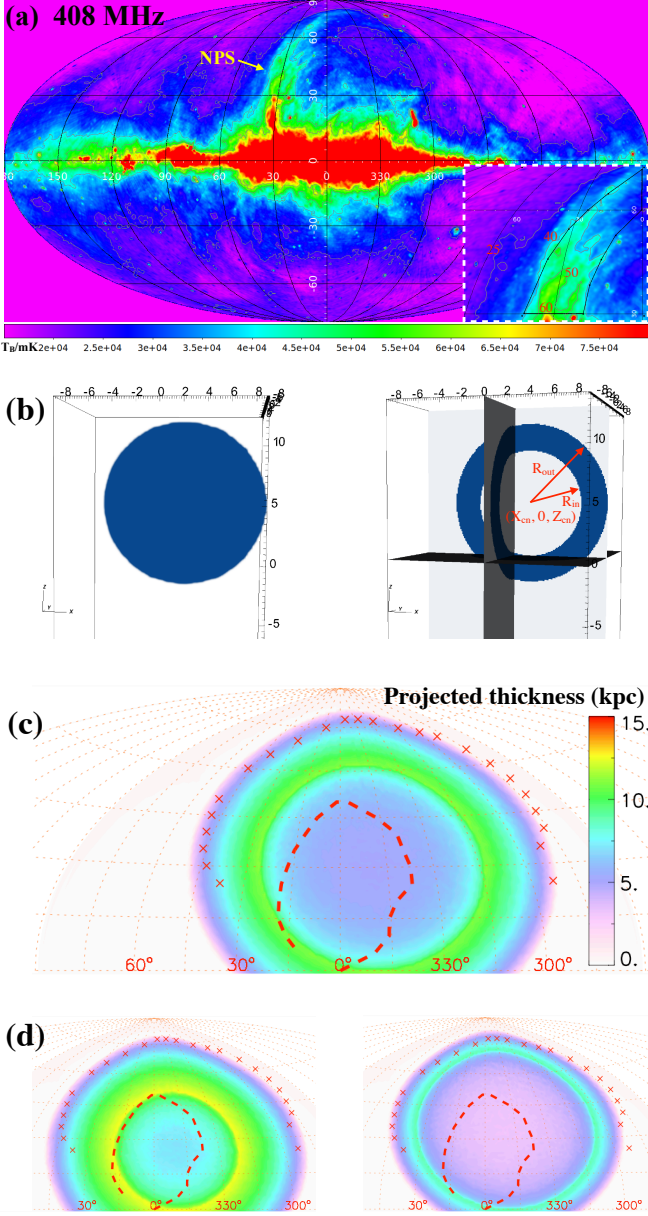


Fig. 1. Panel (a) shows the 408 MHz sky map (Haslam et al. 1982, T_B in mK), with grey contours indicating $T_B = 25$ K, 40 K and 60 K. The right window shows the zoom-in view of the NPS, and the polygon marks the region for radio intensity statistics (similar to the region for gamma-ray analysis in Jóhannesson & Porter 2021). Panel (b) shows the 3D view and the three-slice view of the shell (coordinate values are in units of kpc). Panel (c) shows the projected thickness (D_s) of the radiative shell accounting for the NPS/Loop I in Galactic coordinates with $(R_{in}, R_{out}) = (5.0 \text{ kpc}, 7.5 \text{ kpc})$. The crosses and the dashed line mark the outlines of Loop I and northern Fermi bubble, respectively (see Su et al. 2010 for coordinates). Panel (d) show the projected thickness maps for $(R_{in}, R_{out}) = (4.0 \text{ kpc}, 7.5 \text{ kpc})$ (left) and $(6.0 \text{ kpc}, 7.5 \text{ kpc})$ (right).

decays into gamma rays, $\sigma_{pp} \sim 30 \text{ mb}$ is the cross section of inelastic collision (Aharonian 2004), e_{crp} is the energy density of CRp. X-ray observations suggest that the density and temperature of the hot gas in NPS are $n_{gas} \sim (3 - 4) \times 10^{-3} \text{ cm}^{-3}$ and 0.3 keV, respectively (Kataoka et al. 2013, 2015). If taking the thermal energy density of the ions as the upper limit of e_{crp} , we would have the gamma-ray intensity of $J_\gamma = (4\pi)^{-1} j_\gamma D_s <$

$1 \times 10^3 \text{ eV cm}^{-2} \text{ s}^{-1} \text{ sr}^{-1}$, of which the upper limit is about half of the observed value (Jóhannesson & Porter 2021). Thus, hadronic origin requires relatively extreme conditions of which the energy density of CRp could exceed that of thermal ions, and we believe that gamma rays of the NPS are more likely from ICS.

In ICS, the rate of gamma-ray production per unit volume per unit energy is given by:

$$\frac{dN_\gamma(E_\gamma)}{dE_\gamma} = c \int_{\gamma_e} \int_{E_{ph}} \frac{d\sigma_{IC}(E_\gamma, E_e, E_{ph})}{dE_\gamma} \frac{dN_{cre}}{d\gamma_e} d\gamma_e \frac{dn_{ph}}{dE_{ph}} dE_{ph} \quad (2)$$

where $dN_{cre}/d\gamma_e$ is the energy distribution of primary CRE (see equation 1), dn_{ph}/dE_{ph} is the number density of interstellar radiation field (ISRF) photon per unit energy. The differential cross sections of ICS in above equation can be approximated by $d\sigma_{IC}/dE_\gamma = 3\sigma_T(E_e\Gamma_e)^{-1}[2q \ln q + (1+2q)(1-q) + (\Gamma_e q)^2(1-q)(2+2\Gamma_e q)^{-1}]$, where σ_T is the Thomson cross section, $\Gamma_e \equiv 4E_{ph}E_e/(m_e^2c^4)$, and $q \equiv E_\gamma\Gamma_e^{-1}(E_e - E_\gamma)^{-1}$ (Blumenthal & Gould 1970). The gamma-ray flux is found from the source term (equation 2) as a sightline integral:

$$\frac{dN_\gamma}{dE_\gamma} = \frac{1}{4\pi} \int \frac{dN_\gamma}{dE_\gamma} dR. \quad (3)$$

The ISRF takes the values in GALPROP² v54 (see Figure A1, Moskalenko et al. 2006; Porter et al. 2006). The line-of-sight towards the NPS will pass through different regions, involving different ISRF. Here we take the ISRF at $(R, z) = (5 \text{ kpc}, 5 \text{ kpc})$ as the seed photon in the fiducial case (R is the galactocentric distance and z is the height from the midplane of the Galactic disk).

2.4. Radio NPS

For the radio NPS (Figure 1a), we selected the similar region to the one used in gamma-ray analysis (Jóhannesson & Porter 2021), and simply chose the region of longitude $l = 60^\circ$ (outside and close to the NPS) as the radio background/foreground, of which $T_B \sim 22 \text{ K}$ at 408 MHz. Subtracting the background/foreground of the same latitudes, we derived that the average brightness temperature of the NPS at 408 MHz is $T_B = 20 \text{ K}$. After fitting the gamma-ray spectrum, we obtained a serial of CRE's SEDs with different E_{br} and N_0 . Then for each SED, we calculated the synchrotron emission with different field strength, in which the pitch angle between electron velocity and the field is assumed to be random. We defined the radio-fit conditions as follows: matching the intensity at 408 MHz, spectral indices of $\bar{\alpha}_1 = -0.55 \sim -0.60$ (45–408 MHz) and $\bar{\alpha}_2 = -1.0 \pm 0.1$ (0.408–23 GHz), in which $\bar{\alpha}_1 \equiv \ln(S_{45\text{MHz}}/S_{408\text{MHz}})/\ln(45/408)$ and $\bar{\alpha}_2 \equiv \ln(S_{408\text{MHz}}/S_{23\text{GHz}})/\ln(0.408/23)$. These conditions restrict the model parameters to a narrow range.

2.5. Results

By modeling the radio and gamma-ray data, we choose the setup with $p = 2.0$ and $E_{br} = 4 \text{ GeV}$ as the fiducial case (Table 1 and Figure 2). The coefficients of CRE SED (equation 1) in the fiducial case are $N_0 = 5.6 \times 10^{-9} \text{ cm}^{-3}$ and $N_1 = 4.4 \times 10^{-5} \text{ cm}^{-3}$. The energy density of CRE is thus $e_{cre} = 3.9 \times 10^{-14} \text{ erg cm}^{-3}$, and the number density of CRE

² <http://galprop.stanford.edu>

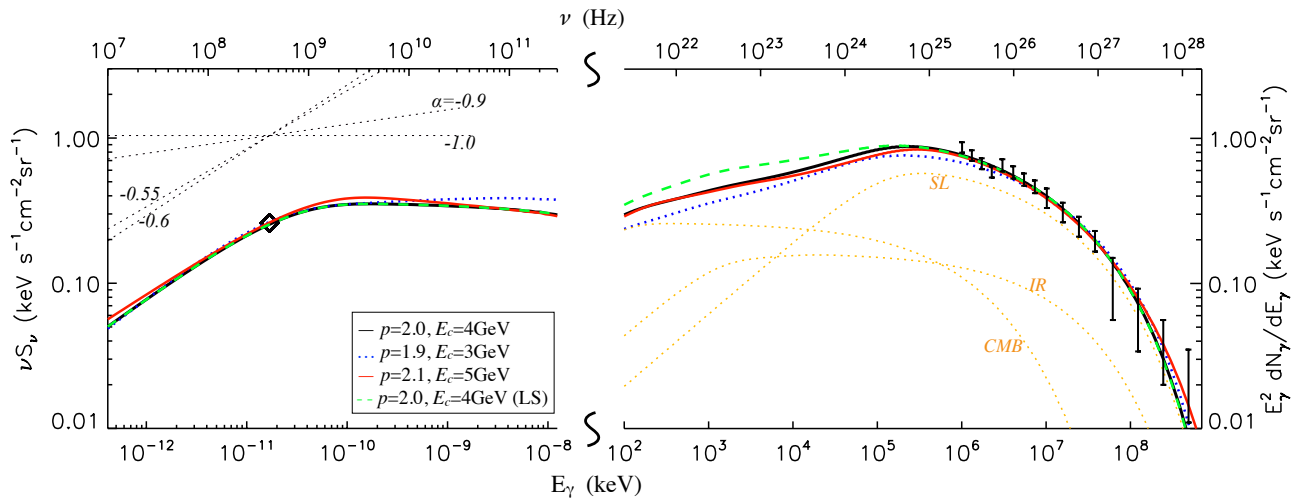


Fig. 2. Modeling the radio and gamma-ray spectra for the NPS. The diamond and errorbars mark radio intensity (408 MHz) and gamma-ray data (Jóhannesson & Porter 2021) of the NPS, respectively. The orange dotted lines indicate the radiation of the ICS on different components of the ISRF for $p = 2.0$ (SL – star light; IR – infrared; CMB – cosmic microwave background. See figure A1 for details).

Table 1. Parameters for modeling the radio and gamma-ray NPS. Note: “Y” or “N” (yes or no) behind the E_c -value indicates whether the values of modeled $\bar{\alpha}_1$ and $\bar{\alpha}_2$ meet the radio-fit conditions, and “LS” behind the p -value marks the local structure scenario.

| p | E_{br} GeV | N_0 cm^{-3} | e_{cre} erg cm^{-3} | B μG | $\bar{\alpha}_1$ | $\bar{\alpha}_2$ |
|-------|-----------------|---------------------------|-----------------------------------|----------------------|------------------|------------------|
| 1.9 | 3 (Y) | 1.9×10^{-9} | 2.4×10^{-14} | 4.3 | -0.58 | -0.91 |
| 2.0 | 3.5 (N) | 5.6×10^{-9} | 3.9×10^{-14} | 3.5 | -0.61 | -0.95 |
| 2.0 | 4 (Y) | 4.9×10^{-9} | 3.5×10^{-14} | 3.8 | -0.59 | -0.93 |
| 2.0 | 5 (N) | 3.9×10^{-9} | 2.9×10^{-14} | 4.2 | -0.56 | -0.88 |
| 2.1 | 4 (N) | 1.3×10^{-8} | 5.5×10^{-14} | 3.6 | -0.63 | -0.97 |
| 2.1 | 5 (Y) | 1.0×10^{-8} | 4.5×10^{-14} | 4.0 | -0.60 | -0.92 |
| 2.1 | 6 (N) | 8.6×10^{-9} | 3.8×10^{-14} | 4.4 | -0.59 | -0.88 |
| 2.2 | 7 (N) | 2.5×10^{-8} | 6.8×10^{-14} | 3.9 | -0.63 | -0.90 |
| 1.9LS | 3 (Y) | 1.7×10^{-7} | 2.1×10^{-12} | 4.3 | -0.58 | -0.91 |
| 2.0LS | 4 (Y) | 4.4×10^{-7} | 3.2×10^{-12} | 3.8 | -0.59 | -0.93 |
| 2.1LS | 5 (Y) | 9.0×10^{-7} | 3.9×10^{-12} | 4.1 | -0.60 | -0.92 |
| 2.2LS | 7 (N) | 2.3×10^{-6} | 6.3×10^{-12} | 3.9 | -0.63 | -0.90 |

is $\sim 2.5 \times 10^{-9} \text{ cm}^{-3}$, which is 10^{-6} of the thermal density derived from X-ray observations (Kataoka et al. 2013). In addition, the energy density of CRe is about 6% of that of the magnetic field, indicating a significant deviation from energy equipartition between the CRe and the magnetic field.

We also derived the confidence intervals of the CRe’s parameters beyond which the radio-fit conditions will never be met: $E_{br} \approx 3 \text{ GeV}$ for $p = 1.9$, $3.5\text{--}5 \text{ GeV}$ for $p = 2.0$, and 5 GeV for $p = 2.1$ (Table 1). The radio conditions rule out the cases of $p \geq 2.2$ and $p \leq 1.8$. Thus, the possible range of e_{cre} would be $(2.4\text{--}4.5) \times 10^{-14} \text{ erg cm}^{-3}$.

The gamma-ray of the NPS is dominated by the ICS on the star light (Figure 2). Since the star light dilutes with the height from the Galactic disk, this is in agreement with dimming of the gamma-ray NPS with latitude (e.g., Ackermann et al. 2014).

3. Discussions

According to X-ray observations, the post-shock gas accounting for the X-ray NPS has a temperature of 0.3 keV and a density of $n_{\text{gas}} \approx (3\text{--}4) \times 10^{-3} \text{ cm}^{-3}$ (Kataoka et al. 2015). Thus, the thermal pressure is $P_{\text{th}} \approx 3 \times 10^{-12} \text{ dyn cm}^{-2}$. The CRe acceleration efficiency of the shock defined as the ratio the fraction of shock energy converted into CRe’s energy is $\eta_e \approx e_{cre}/[e_{cre} + e_B + (\gamma - 1)^{-1} P_{\text{th}}] = 0.7\%$ in our fiducial case, suggesting that CRe can be efficiently accelerated by weak shocks. If considering the confidence intervals, η_e would be (0.5–0.9)%. This value is unusually large compared with the expectation of the canonical DSA theory (e.g., $\lesssim 10^{-4}$ for Mach number $\lesssim 3$, Kang & Ryu 2013), but is in agreement with the speculation from observations of some radio relics (e.g., Botteon et al. 2020). Moreover, the Mach number of 1.5 inferred from X-rays (Kataoka et al. 2013) is significantly smaller than that deduced from DSA for $p < 2.2$ ($\mathcal{M} > 4.6$). Thus, the high acceleration efficiency of CRe and flat radio spectra suggest that re-acceleration of CRe should exist for the NPS. **The field strength is around 4 μG , suggesting that the magnetic pressure is about 50 times CRe’s pressure. The plasma beta defined as the thermal-to-magnetic pressure ratio is ~ 5 in the post-shock gas while it is uncertain in the pre-shock gas.**

If energy equipartition between CR and field still holds, for our fiducial case the energy density of CRp would be about 16 times that of CRe ($e_{crp} \sim 5.4 \times 10^{-13} \text{ erg cm}^{-3}$), and the acceleration efficiency would be 11% for CRp. Compared with the DSA mechanism, this remarkably high efficiency implies that CRp may have been re-accelerated by the weak shock as well.

The cooling break energy of CRe (E_{br}) deduced from the radio and gamma-ray spectra is around 5 GeV. Given the ISRF energy density of $1.83 \times 10^{-12} \text{ erg cm}^{-3}$ at $(R, z) = (5 \text{ kpc}, 5 \text{ kpc})$ and the field strength of 4 μG , the cooling timescale for CRe of 4 GeV is 50 Myr, in agreement with the eROSITA bubbles’ age of 20 Myr (Predehl et al. 2020), suggesting that the results in agreement with the premise of halo-structure nature.

For the LS scenario, the energy density of CRe deduced is $(2\text{--}4) \times 10^{-12} \text{ dyn cm}^{-2}$. As a comparison, the pressure of the hot plasma of million Kelvin filling the local hot bubble is estimated to be $\sim 1 \times 10^{-12} \text{ dyn cm}^{-2}$ (Puspitarini et al. 2014; Snowden et al. 2014). The magnetic field measured by Voyager 1 crossing

the heliopause is $\sim 5 \mu\text{G}$ (Burlaga & Ness 2014), while modeling the radio emission at the Galactic plane estimates that the magnetic field at the Solar position should be $\sim 3 \mu\text{G}$ (Jaffe et al. 2010). Let's take the magnetic field of $5 \mu\text{G}$ as the representative value of the local bubble, and assume that CR and magnetic field are in energy equipartition. The total pressure (including thermal pressure, magnetic pressure and CRe pressure) of the local bubble should be $\sim 3 \times 10^{-12} \text{ dyn cm}^{-2}$, which is in line with the value in Cox (2005). Thus, the acceleration efficiency of CRe in the LS scenario would be unusually high, which is a challenge for the current knowledge on the shock acceleration of supernova remnants. **In addition, by integrating over the volume in the LS (see the shell in Figure 1b but scaled down to 0.011 times), the total CRe energy is over $1 \times 10^{50} \text{ erg}$. This value is also extraordinary compared with $10^4 \text{ yr-old SNRs Cygnus Loop and W44, of which the total energies of CRe derived by modeling the radio and gamma-ray data are } \lesssim 1 \times 10^{49} \text{ (Katagiri et al. 2011) and } \sim 10^{48} \text{ erg (Ackermann et al. 2013), respectively.}$**

Acknowledgements. GM thanks Zhongqun Cheng for helpful discussion.

References

- Ackermann, M., Ajello, M., Allafort, A., et al. 2013, *Science*, 339, 807
 Ackermann, M., Albert, A., Atwood, W. B., et al. 2014, *ApJ*, 793, 64
 Aharonian F. A., 2004, *Very High Energy Cosmic Gamma Radiation: A Crucial Window on the Extreme Universe* (River Edge, NJ: World Scientific)
 Beck, R., & Krause, M., 2005, *Astron. Nachr.*, 326, 414
 Bell, A. R. 1978, *MNRAS*, 182, 443
 Bennett, C. L., Hill, R. S., Hinshaw, G., et al. 2003, *ApJS*, 148, 97
 Bland-Hawthorn J., Gerhard O., 2016, *ARA&A*, 54, 529
 Blasi, P. 2013, *ARA&A*, 21, 70
 Blumenthal, G. R., & Gould, R. J. 1970, *Rev. Mod. Phys.*, 42, 237
 Botteon A., Brunetti G., Ryu D., Roh S., 2020, *A&A*, 634, A64
 Brunetti, G., & Jones, T. W. 2014, *Int. J. Mod. Phys. D*, 23, 1430007
 Burlaga, L. F., & Ness, N. F. 2014, *ApJ*, 784, 146
 Carretti, E., Crocker, R. M., Staveley-Smith, L., et al. 2013, *Nature*, 493, 66
 Casandjian, J. M., & Grenier, I. 2009, arXiv: 0912.3478
 Cox, D. P. 2005, *ARA&A*, 43, 337
 Das, K. K., Zucker, C., Speagle, J. S., et al. 2020, *MNRAS*, 498, 5863
 De Oliveira-Costa, A., Tegmark, M., Gaensler, B.M., et al. 2008, *MNRAS*, 388, 247
 Di Gennaro, G., van Weeren, R., Hoeft, M., et al. 2018, *ApJ*, 865, 24
 Giuliani, A., Cardillo, M., Tavani, M., et al. 2011, *ApJ*, 742, L30
 Guo, F., & Mathews, W. G. 2012, *ApJ*, 756, 181
 Guzmán, A. E., May, J., Alvarez, H., & Maeda, K. 2011, *A&A*, 525, A138
 Haslam C. G. T., Salter C. J., Stoffel H., Wilson W. E., 1982, *A&AS*, 47, 1
 Jaffe, T. R., Leahy, J. P., Banday, A. J., et al. 2010, *MNRAS*, 401, 1013
 Jew, L., & Grumitt, R. D. P. 2020, *MNRAS*, 495, 578
 Jóhannesson, G., & Porter, T. A. 2021, *ApJ*, 917, 30
 Large, M. I., Quigley, M. J. S., Haslam, C. G. T., 1962, *MNRAS*, 124, 405
 Locatelli, N. T., Rajpurohit, K., Vazza, F., et al., 2020, *MNRAS*, 496, L48
 Kang H., & Ryu D., 2011, *ApJ*, 734, 18
 Kang, H., Ryu, D. & Jones, T. W. 2012, *ApJ*, 756, 97
 Kang, H., & Ryu, D. 2013, *ApJ*, 764, 95
 Katagiri, H., Tibaldo, L., Ballet, J., et al. 2011, *ApJ*, 741, 44
 Kataoka, J., Tahara, M., Totani, T., et al. 2013, *ApJ*, 779, 57
 Kataoka, J., Tahara, M., Totani, T., et al. 2015, *ApJ*, 807, 77
 Miville-Deschênes, M.-A., Ysard, N., Lavabre, A., et al. 2008, *A&A*, 490, 1093
 Morlino, G., & Caprioli, D. 2012, *A&A*, 538, A81
 Moskalenko, I. V., Porter, T. A., & Strong, A. W. 2006, *ApJ*, 640, L155
 Mou, G., Yuan, F., Bu, D., et al. 2014, *ApJ*, 790, 109
 Mou, G., Sun, D., & Xie, F. 2018, *ApJ*, 869, L20
 Mou, G., Sun, D., Fang, T., et al. 2022, submitted.
 Panopoulou, G. V., Dickinson, C., Readhead, A. C. S., et al. 2021, *ApJ*, 922, 210
 Pinzke, A., Oh, S. P., & Pfrommer, C. 2013, *MNRAS*, 435, 1061
 Platania, P., Burigana, C., Maino, D., et al. 2003, *A&A*, 410, 847
 Porter, T. A., Moskalenko, I. V., & Strong, A. W. 2006, *ApJ*, 648, L29
 Predehl, P., Sunyaev, R. A., Becker, W., et al., 2020, *Nature*, 588, 227
 Puspitarini, L., Lallement, R., Vergely, J. L., & Snowden, S. L. 2014, *A&A*, 566, A13
 Sarkar, K. C. 2019, *MNRAS*, 482, 4813
 Sironi L., Giannios D., 2013, *ApJ*, 778, 107

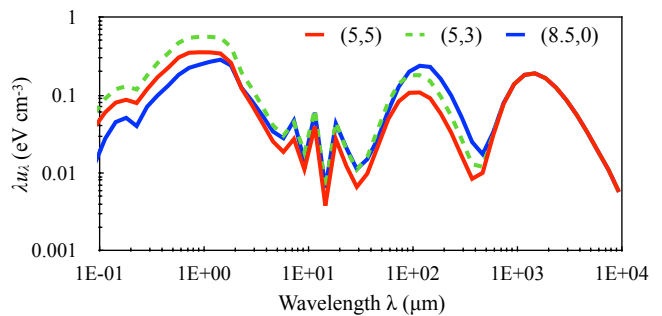


Fig. A1. ISRF at three positions: $(R, z)=(5 \text{ kpc}, 5 \text{ kpc})$, $(8.5 \text{ kpc}, 0)$ and $(5 \text{ kpc}, 3 \text{ kpc})$.

- Snowden, S. L., Egger, R., Freyberg, M. J., et al. 1997, *ApJ*, 485, 125
 Snowden, S. L., Chiao, M., Collier, M. R., et al. 2014, *ApJ*, 791, L14
 Sofue, Y. 1977, *A&A*, 60, 327
 Sofue, Y. 2000, *ApJ*, 540, 224
 Sofue, Y., 2015, *MNRAS*, 447, 3824
 Sofue, Y., Habe, A., Kataoka, J., et al. 2016, *MNRAS*, 459, 108
 Sofue, Y. 2019, *MNRAS*, 484, 2954
 Su, M., Slatyer, T. R., & Finkbeiner, D. P. 2010, *ApJ*, 724, 1044
 van Weeren, R. J., Andrade-Santos, F., Dawson, W. A., et al. 2017, *NatAs*, 1, 0005
 van Weeren, R. J., de Gasperin, F., Akamatsu, H., et al. 2019, *SSRv*, 215, 16
 Vazza, F., Eckert, D., Brügger, M., & Huber, B. 2015, *MNRAS*, 451, 2198
 Vidal, M., Dickinson, C., Davies, R. D., & Leahy, J. P. 2015, *MNRAS*, 452, 656
 Weaver, H. 1979, in *IAU Symp. 84, The Large-Scale Characteristics of the Galaxy*, ed. W. B. Burton (Dordrecht: Reidel), 295
 Wolleben, M. 2007, *ApJ*, 664, 349